

Chapter 1

3-D example

INTRODUCTION

In Chapter ?? and ?? I introduced the concept of tau tomography in steering filter preconditioning. I showed how, on a simple synthetic, using tau tomography preconditioned with steering filters provided superior velocity estimation compared to conventional methods. In Chapter ?? I applied the methodology on a 2-D line taken from a 3-D North Sea dataset. The velocity estimated by my tomography methodology proved superior to both the conventional layer- and grid-based approaches.

In this chapter, I apply the same methodology, tau tomography with steering filter preconditioning, to estimate a 3-D velocity function for the North Sea dataset introduced in Chapter ??. I begin by introducing the dataset and explaining the preprocessing. I then show the result of applying Common Azimuth Migration (CAM) (Biondi and Palacharla, 1996) to the dataset using a layer-base velocity estimate. I pick several reflectors representing major structural boundaries. I perform semblance analysis using these reflectors. I calculate the dips along the picked reflectors and, using the methodology described in Appendix ??, I construct a 3-D steering filter. I invert for a new velocity using the 3-D tau tomography operator described in Appendix ??. I conclude by remigrating the dataset with the updated velocity model. The updated migration shows more reflector coherency and overall better focusing.

DATA

In this section I discuss the acquisition and preprocessing of the L7D dataset.

Acquisition Parameters

The data were acquired over a salt dome in the North Sea using three cables of 3570m length with geophones every 25m. The CMP sampling inline was 13.33m and crossline of 25m. The entire survey covered 13.5km inline and 4km crossline.

Preprocessing

As mentioned in Chapter ??, Kirchhoff methods are normally used when performing migration velocity analysis. As in the previous chapters, I chose instead to use a wave equation method to construct my CRP gathers. Figure 1.1 shows source locations and offset-azimuth distribution for a portion of the L7D dataset. The irregularity of both domains imposes a problem. Wave equation methods require the data to be on a regular mesh. There are several methods to regularize the geometry with the usual tradeoff of accuracy vs. cost. Two common choices are relatively inexpensive: partial stacking (Hanson and Witney, 1995) and the more accurate Azimuth Moveout (AMO) introduced by Biondi et al. (1998).

AMO is a partial migration operator and can be thought of as a cascade of Dip Moveout (DMO) (Hale, 1983) and inverse DMO (Ronen, 1985). It attempts to construct data at a given offset-azimuth pair by applying a relatively small, and therefore relatively inexpensive, operator. AMO can construct regularly sampled data from the irregular trace locations shown in Figure 1.1. In this chapter I will be using the regular data cube constructed by Vaillant and Calandra (2000). In the process of performing AMO the dataset was resampled. The resampled dataset had CMP spacing of 20m in the inline and 25m in the crossline. The offset range was resampled to 50m ranging from 200m to 3400m.

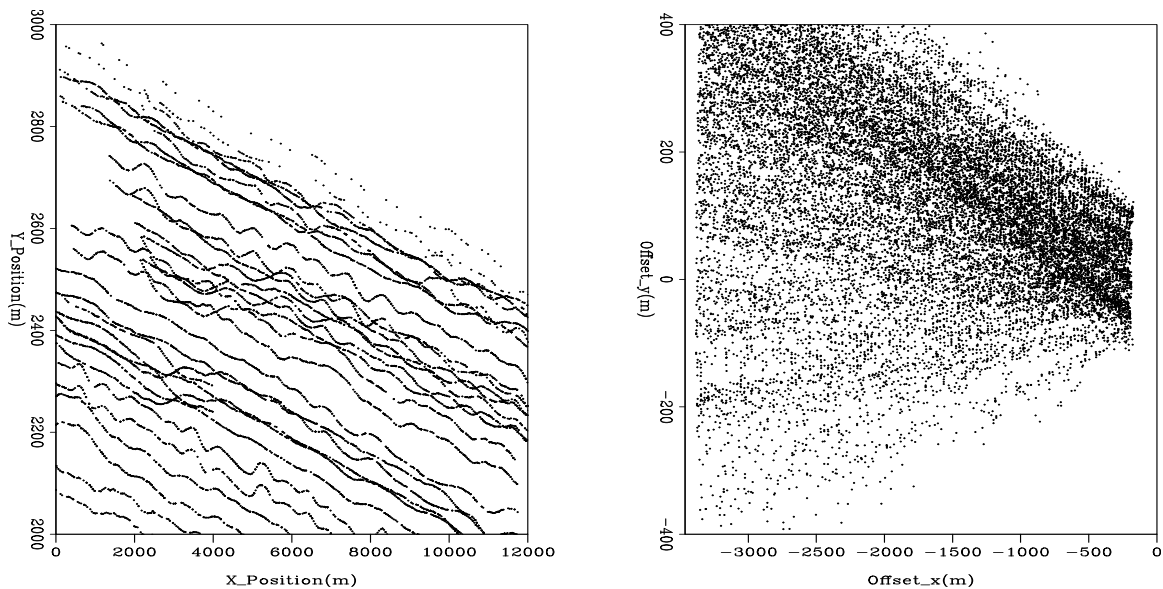
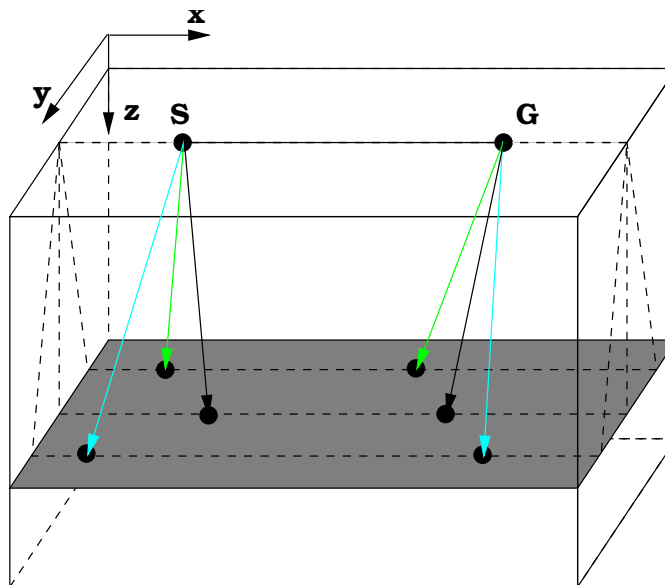


Figure 1.1: The left panel shows the source positions for a portion of the L7D dataset. The right panel shows the offset distribution for the same subset. `3d-amo-cmp` [CR]

Common Azimuth Migration

The cost of full wave equation migration is still prohibitive. As a result, several methods have been developed that sacrifice accuracy for computational efficiency. One method, offset plane wave migration (Ottolini and Claerbout, 1984; Mosher et al., 1997), decomposes the wave field into constant $\frac{kx}{\omega}$ waves and then downward continues each plane wave independently. Unfortunately, offset plane migration quickly deteriorates in media that vary from $v(z)$ (Biondi et al., 1999). I chose to instead use another method that has been developed to do 3-D prestack migration economically, Common Azimuth Migration. In CAM each azimuth is migrated independently, with the assumption that the source and receivers stay in the same plane while being downward continued (Figure 1.2). Vaillant and Biondi (2000) showed that CAM only starts to lose accuracy when beds dip more than 60 degrees at 45 azimuth from the recording geometry. For velocity analysis I felt that this was an acceptable limitation.

Figure 1.2: Geometry of the source and receiver rays for common-azimuth downward continuation. CAM assumes that if the source and receivers are downward continued the downward continued positions will always lay in the same slanted plane. Figure taken from Biondi (1999) `3d-comaz-down` [CR]



INITIAL ERRORS

With the initial velocity model the CRP gathers significant moveout. In this section I show the initial moveout and how I characterize it.

Initial migration

The initial velocity model was created using the S.M.A.R.T¹ method (Jacobs et al., 1992; Ehinger and Lailly, 1995). Early migration tests showed that a better migration result could be obtained by smoothing the model (Vaillant and Sava, 1999). As a result the S.M.A.R.T. model was smoothed, preserving the sharp salt boundary (two slices through the cube are shown in Figure 1.3).

Using the velocity in Figure 1.3, the data was migrated with six reference velocities and frequency range of 5 to 60 Hz (Vaillant and Sava, 1999; Vaillant and Calandra, 2000). Figures 1.4 and 1.5 show two different slices through the initial migration cube. Note how in

¹Sequential Migration-Aided Reflection Tomography - KIM (Kinematic Inversion Methods), IFP consortium

Figure 1.4 the chalk boundary reflection ('B') varies in amplitude. Further, the reflectors under the salt edge die out ('A'). In addition the syncline and fault structure to the right of the salt ('C' and 'D') lack crispness and some reflector continuity. In the second view, Figure 1.5, we again see the problems with the chalk boundary ('B'). As reflectors approach the salt edge they seem to lose coherency ('A' and 'D'). The valley to the right also has problems. Reflectors seem to blur together in both the inline view ('C') and the depth slice ('E'). If we look at the gathers we still see significant moveout errors (Figure 1.6) that the tomography can attempt to correct.

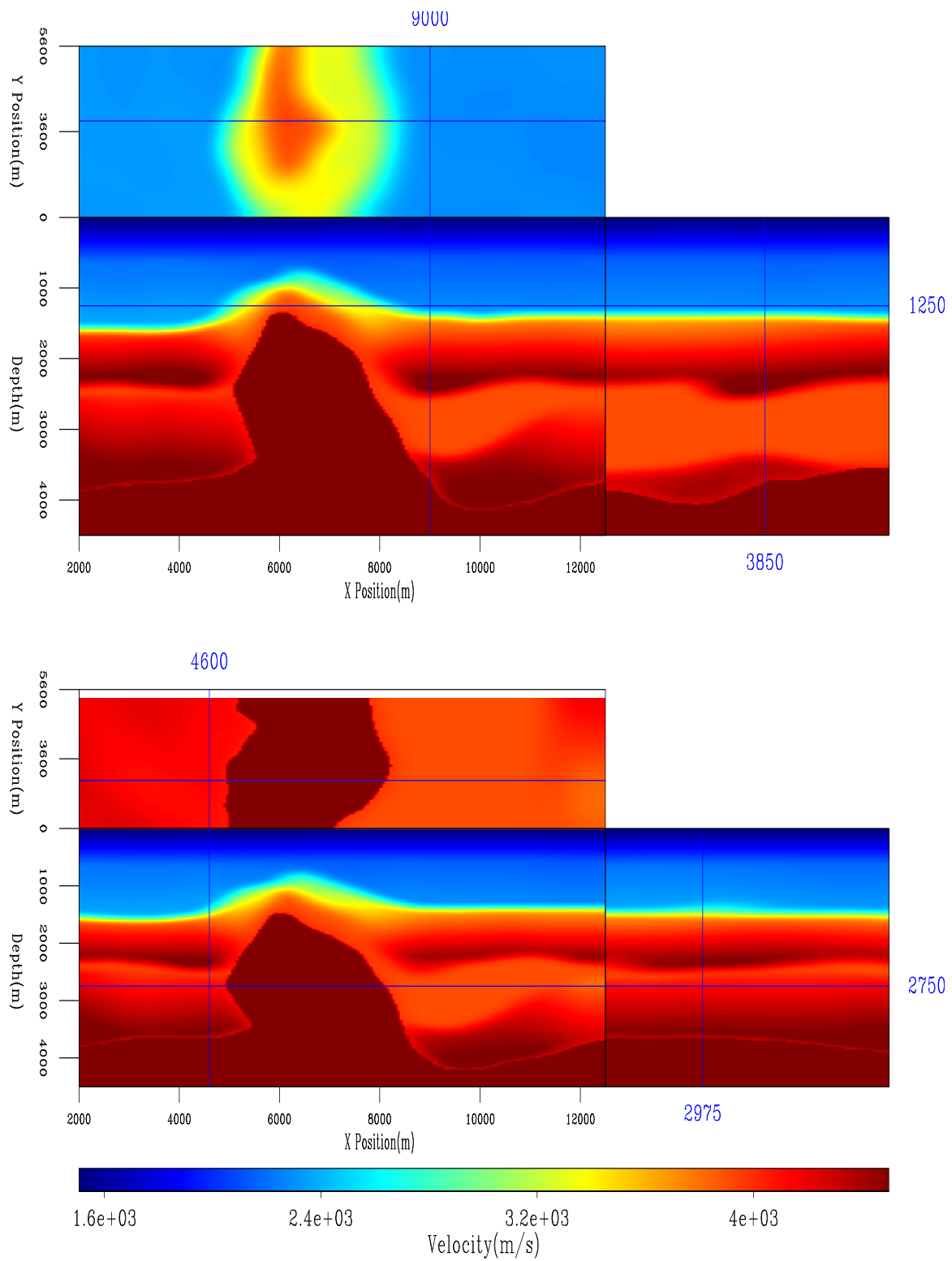
Moveout errors

From the initial migration I chose thirteen reflectors to perform tomography with (Figure 1.7). To constrain the upper portion of the model I chose the sea bottom reflection and the chalk boundary reflection. I chose the salt top and bottom reflection along with four reflectors to the left and five to the right of the salt body. The volume of data made accurate picking of the reflectors difficult especially under the salt edge. As a result, I concentrated more on the area right of the salt where reflector coherency was good in the initial migration.

I performed moveout analysis using equation (??) and extracted the moveout along the thirteen reflectors. Figure 1.8 shows slices through the bottom 12 reflector semblance cubes. Generally the chalk reflector (top-left) showed little to no moveout errors. The remaining eleven showed varying degree of residual moveout. I then created smooth semblance error maps using fitting goals similar to (??), replacing the 1-D differential operator with the Laplacian. Figure 1.9 shows the resulting semblance maps for the same 12 reflectors as Figure 1.8.

BUILDING THE STEERING FILTERS

To construct the 3-D steering filter operator, I followed the methodology described in Appendix ?? for cascading two 2-D steering filter operators to form my 3-D steering filter operator. I used the 13 reflectors picked in the last section. To calculate the dip field I began by calculating the slope in the (x, z) and (y, z) planes. I mapped these two dip fields into (x, y, τ)

Figure 1.3: Initial ELF velocity model. `3d-elf3d.vel0` [CR]

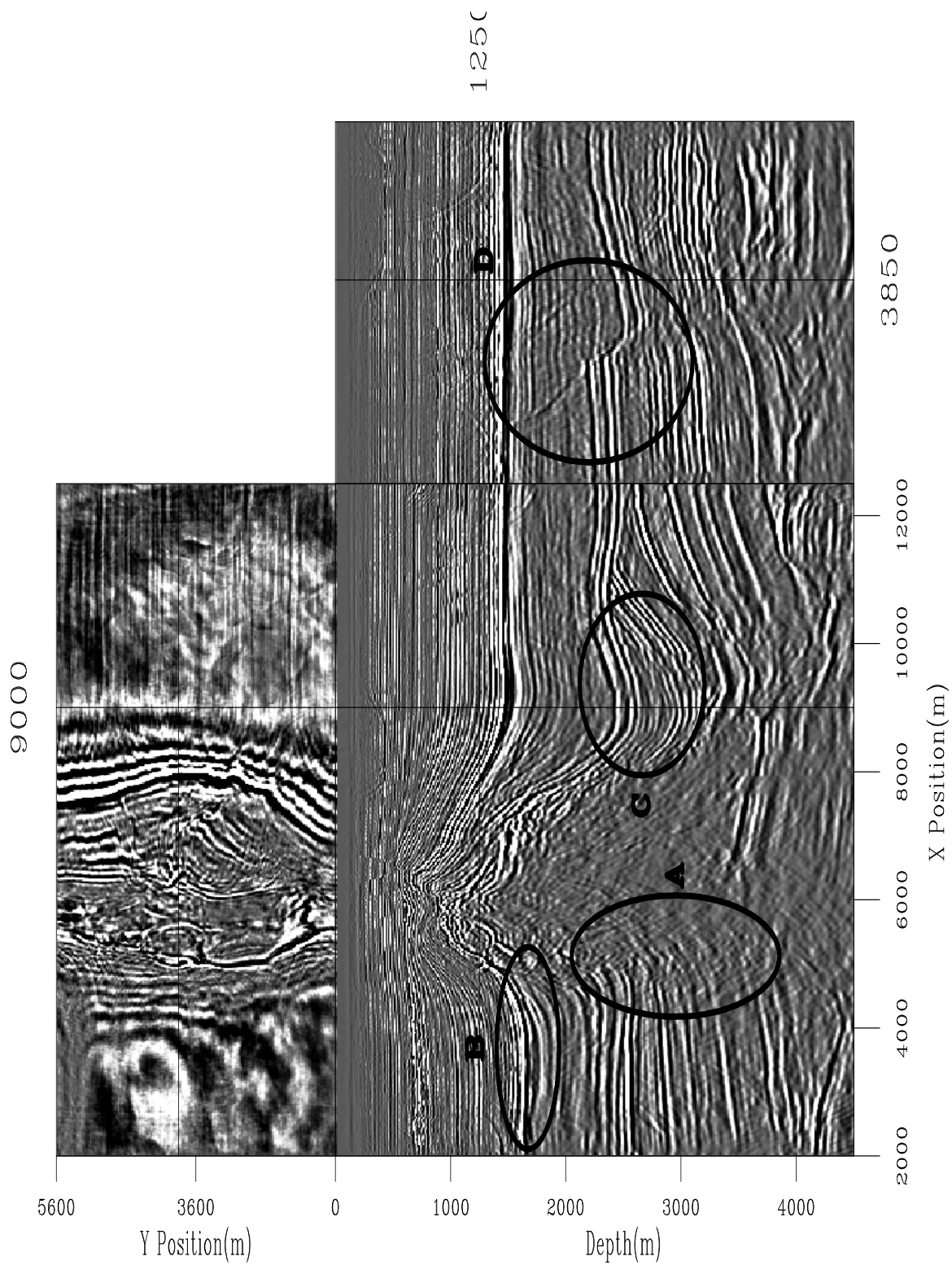


Figure 1.4: Slice through the migrated cube using the velocity of Figure 1.3. 3d-cube.mig0.1 [CR]

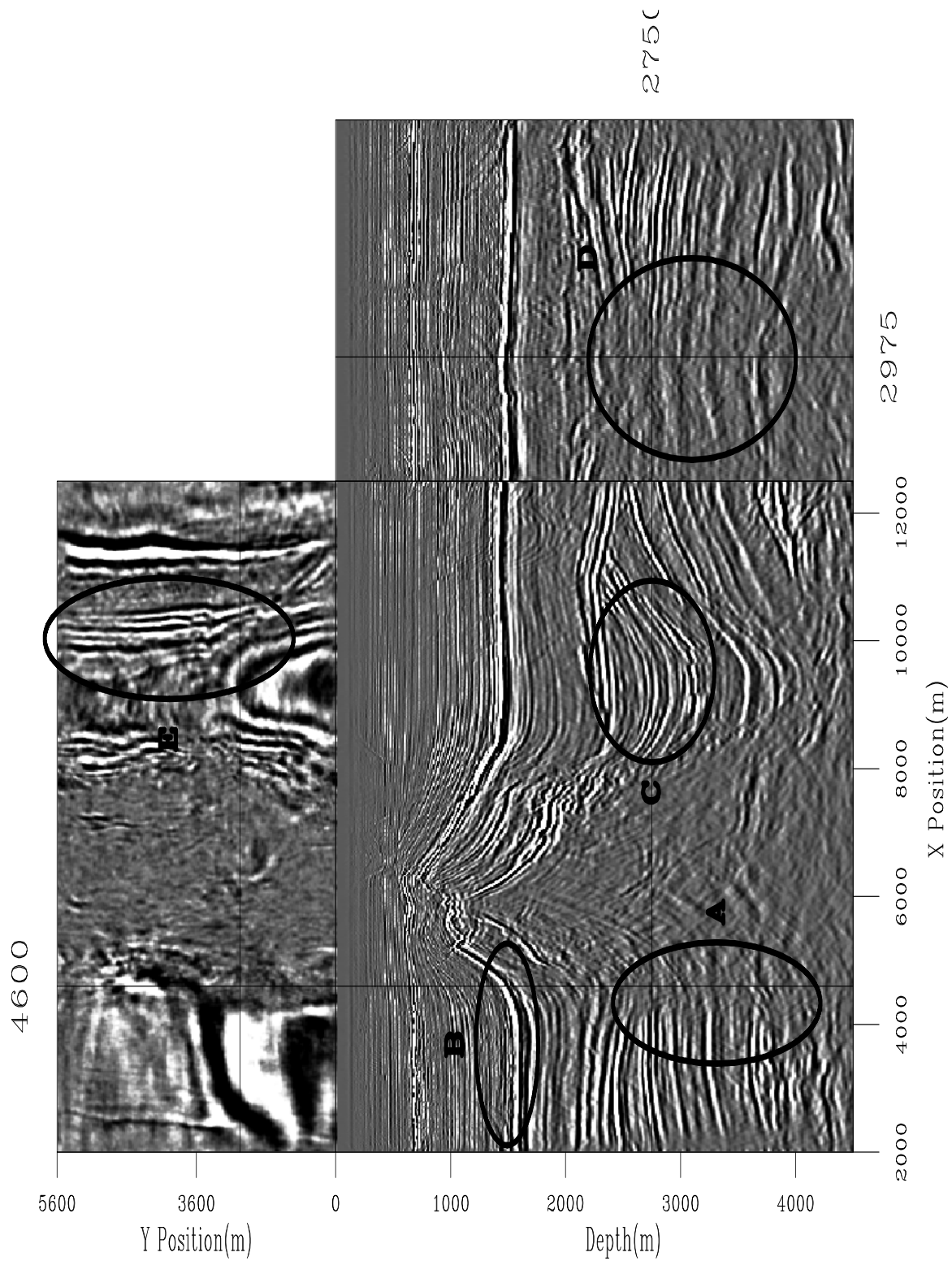


Figure 1.5: A second slice through the migrated cube using the velocity of Figure 1.3.
3d-cube.mig0.2 [CR]

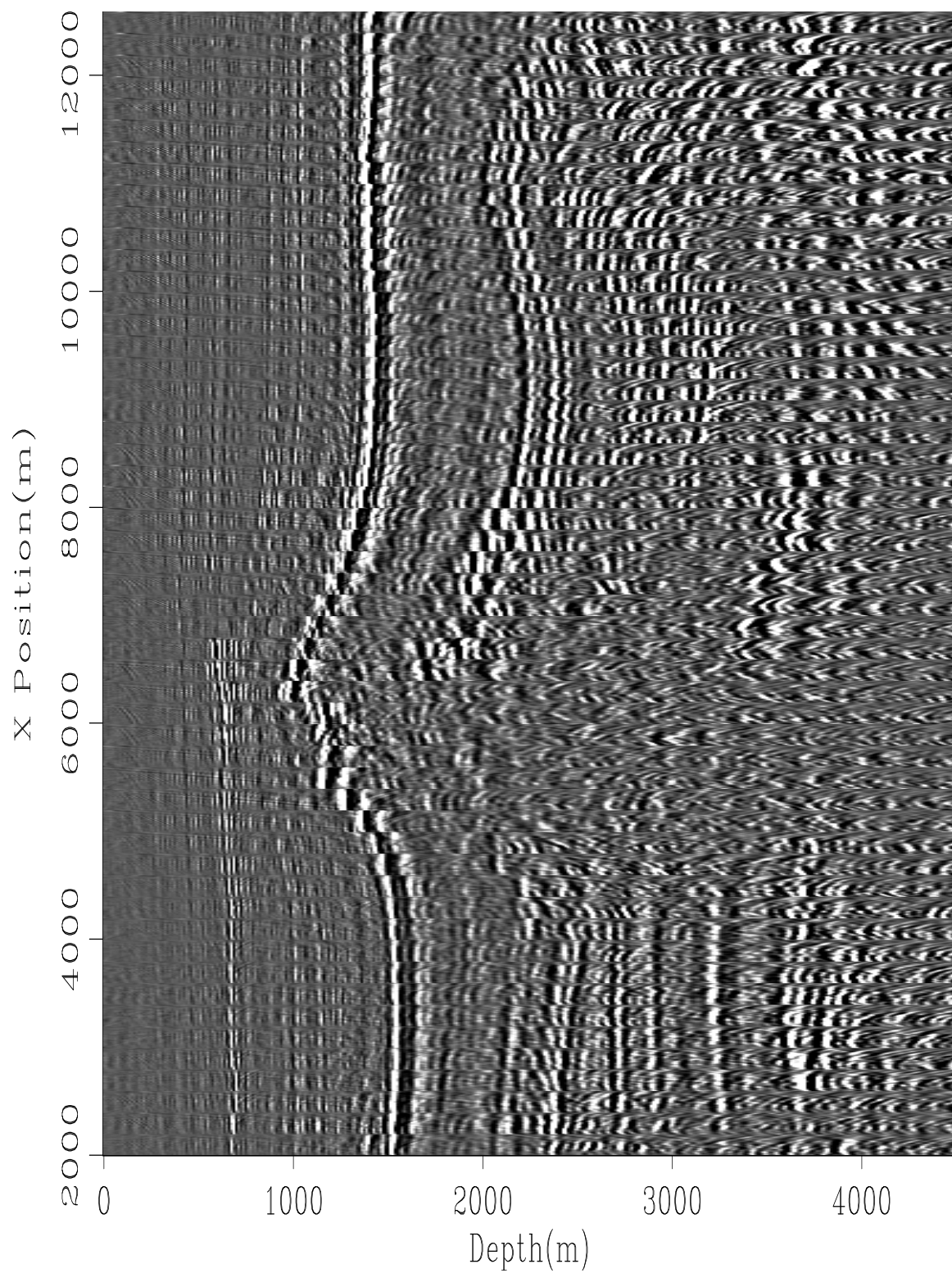


Figure 1.6: Every 10th gather from a crossline ($Y = 1900$). `3d-gathers.3d.vel0` [CR]

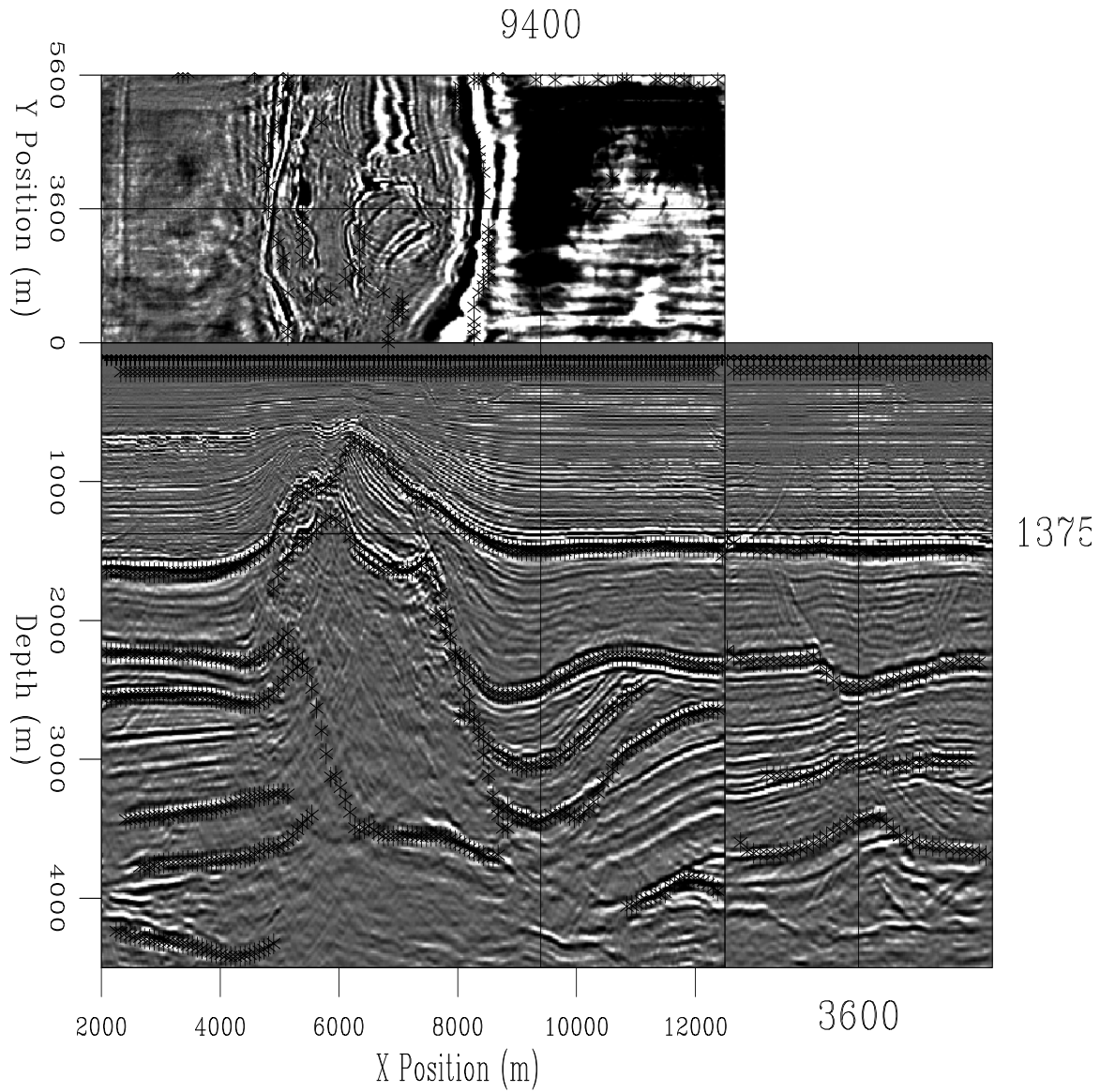


Figure 1.7: The thirteen reflectors used in tomography superimposed on the initial migration image. `3d-elf3d.reflectors.vel0` [CR]

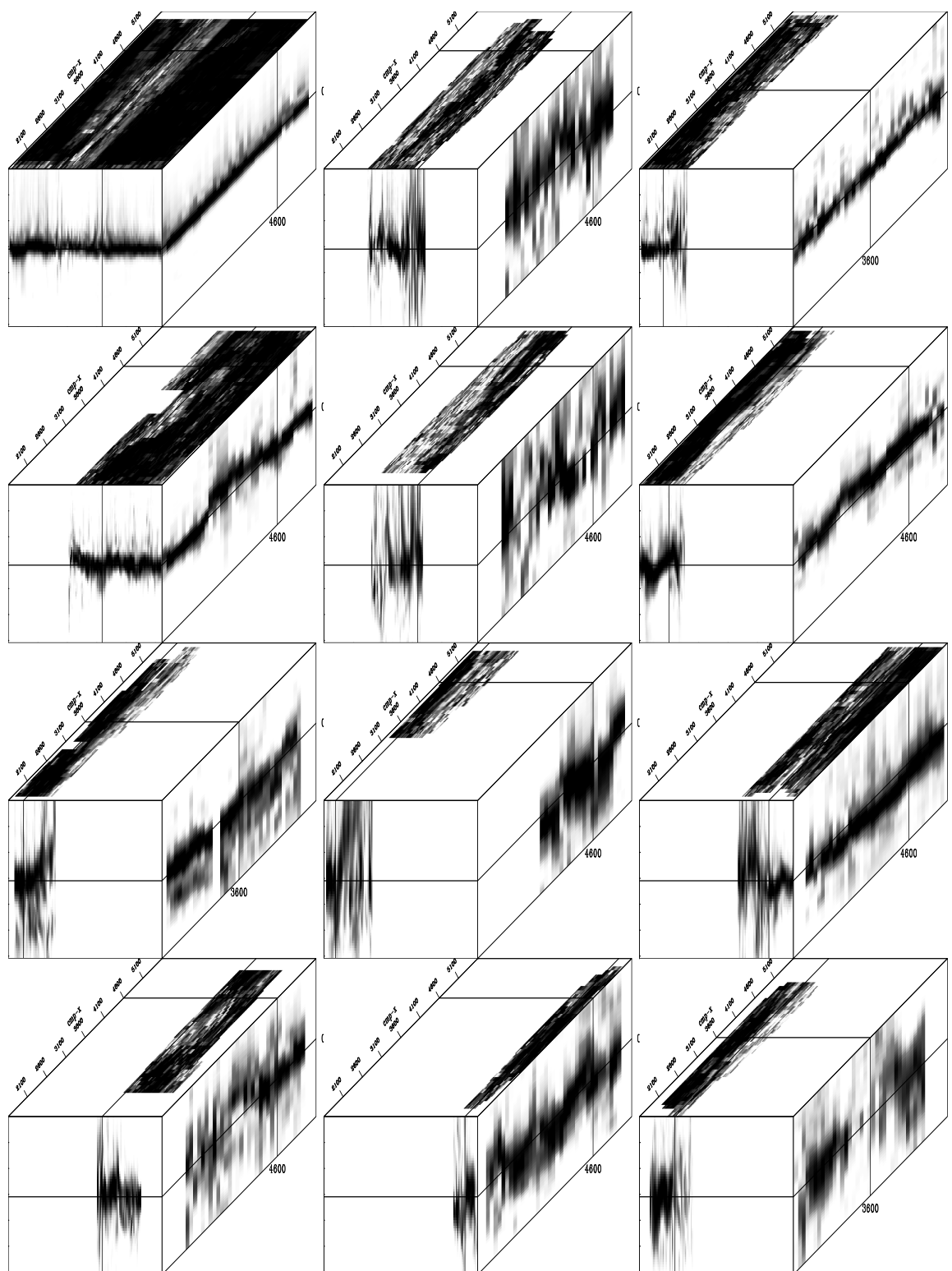


Figure 1.8: Initial moveout semblance along the lower 12 reflectors used in tomography.
`3d-sem-ref.3d` [CR,M]

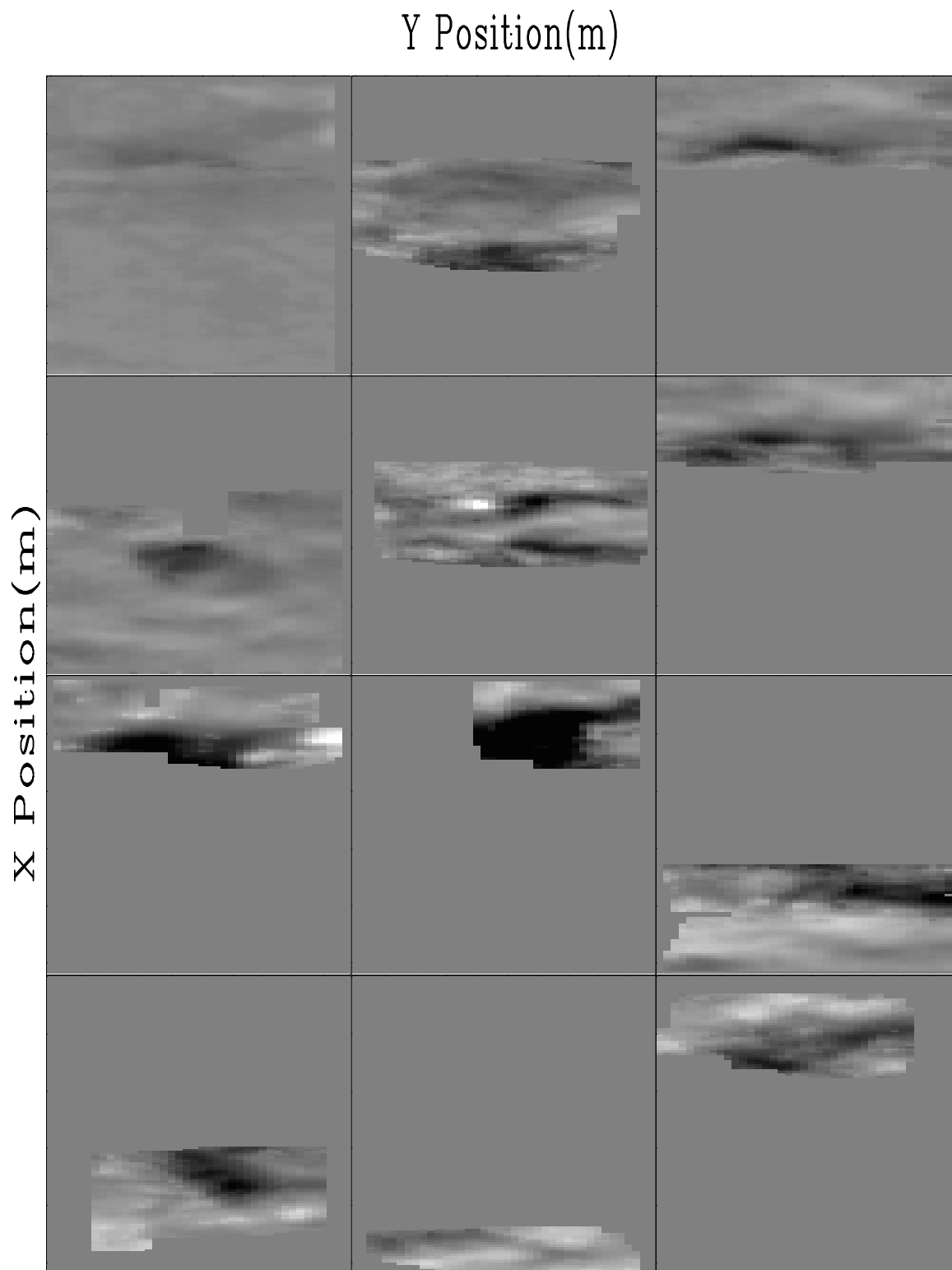


Figure 1.9: Initial moveout semblance along the lower 12 reflectors used in tomography.
`3d-smooth.3d` [CR,M]

model space. I then interpolated the field to the entire model space.

Once I had the dips in both the (x, z) and (y, z) planes I constructed two filter banks which encompassed the range of dips in each direction. It was then a simple matter of creating a mapping operator that mapped the dip at a given model point to a specific filter in the bank. To see the effect of this new complex operator I filled the model with random noise and then applied $A_{3d}A'_{3d}$ (Figure 1.10). As you can see, the 3-D steering filter does a good job in spreading energy along reflector directions.

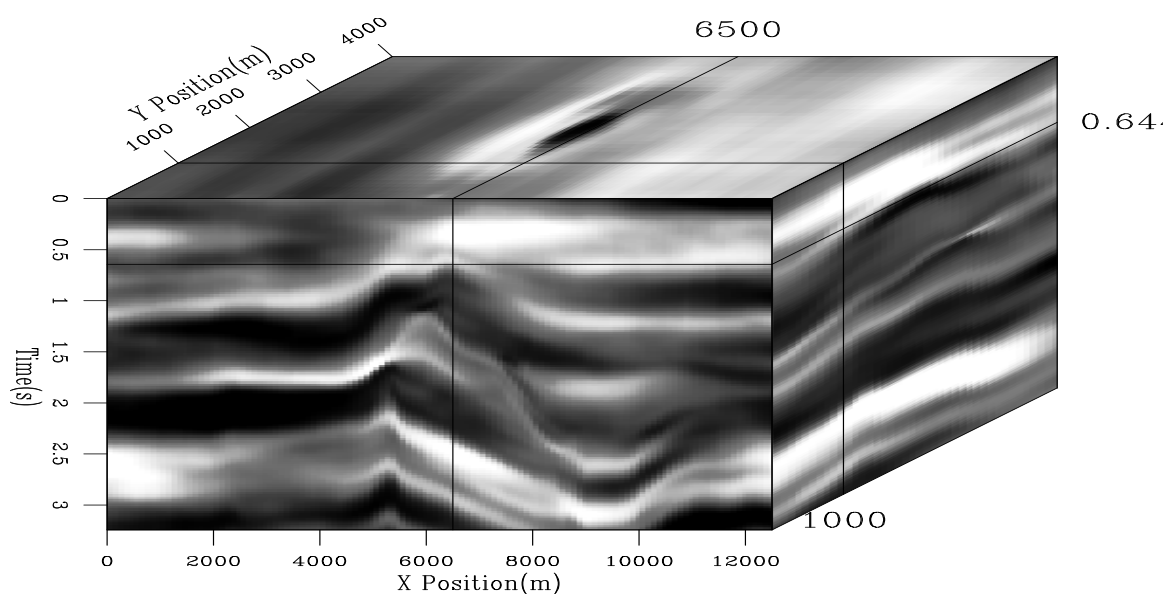


Figure 1.10: The result of putting random numbers into a model then applying $A_{3d}A'_{3d}$.
3d-random-3d [CR,M]

FIRST ITERATION

I applied the fitting goals (??) and obtained a Δs (Figure 1.11). The most dramatic feature of Figure 1.11 is the change in salt position, forcing an increase (black) in the velocity. In addition, note the increase in velocity in the right basin, and a decrease in velocity further to the right. The left portion of the model shows a relatively localized increase in the velocity at approximately 2500 m in depth and 3200 m in the inline.

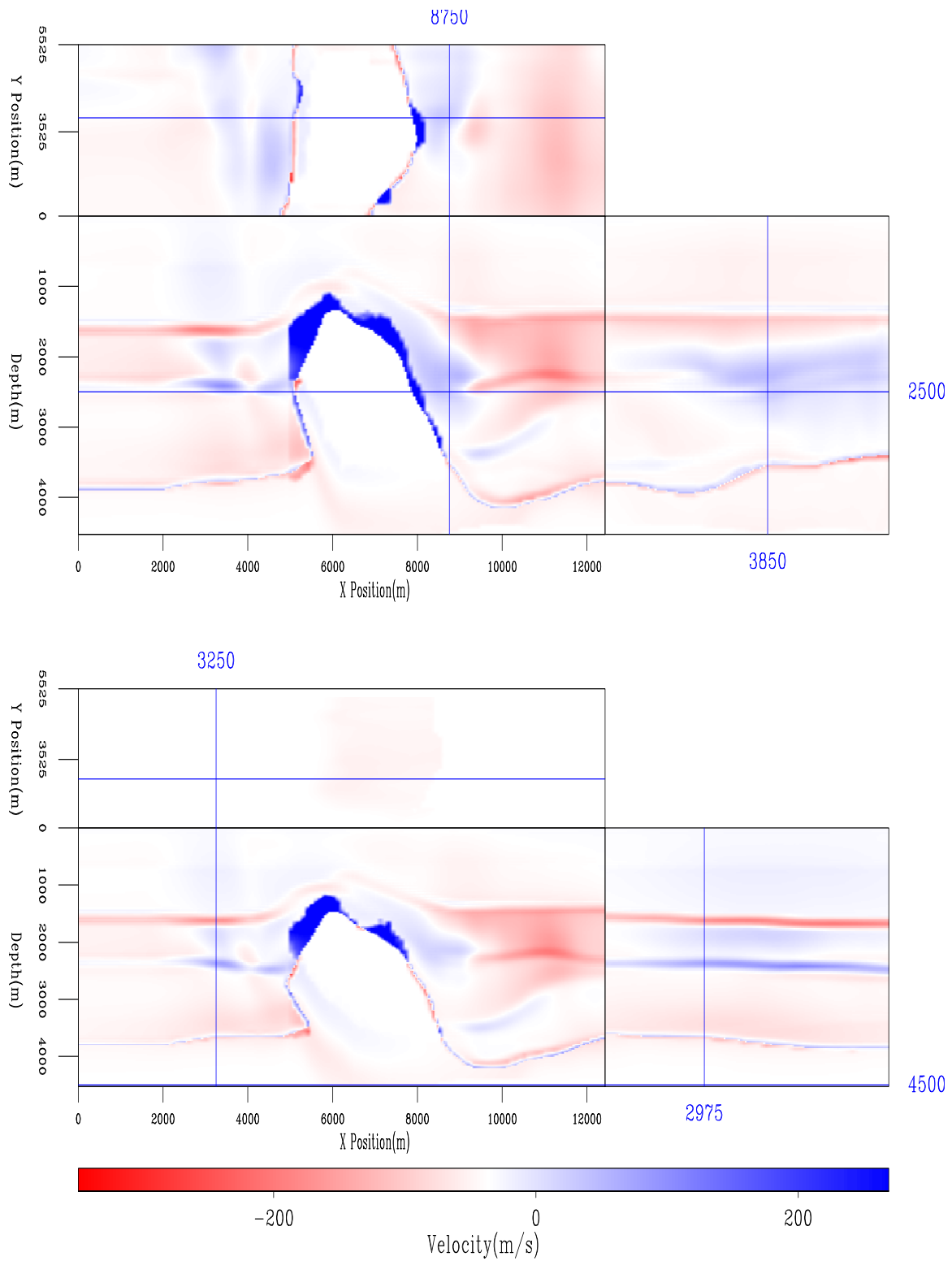


Figure 1.11: Changes to velocity computed from first iteration of tomography. 3d-ds-3d
[CR,M]

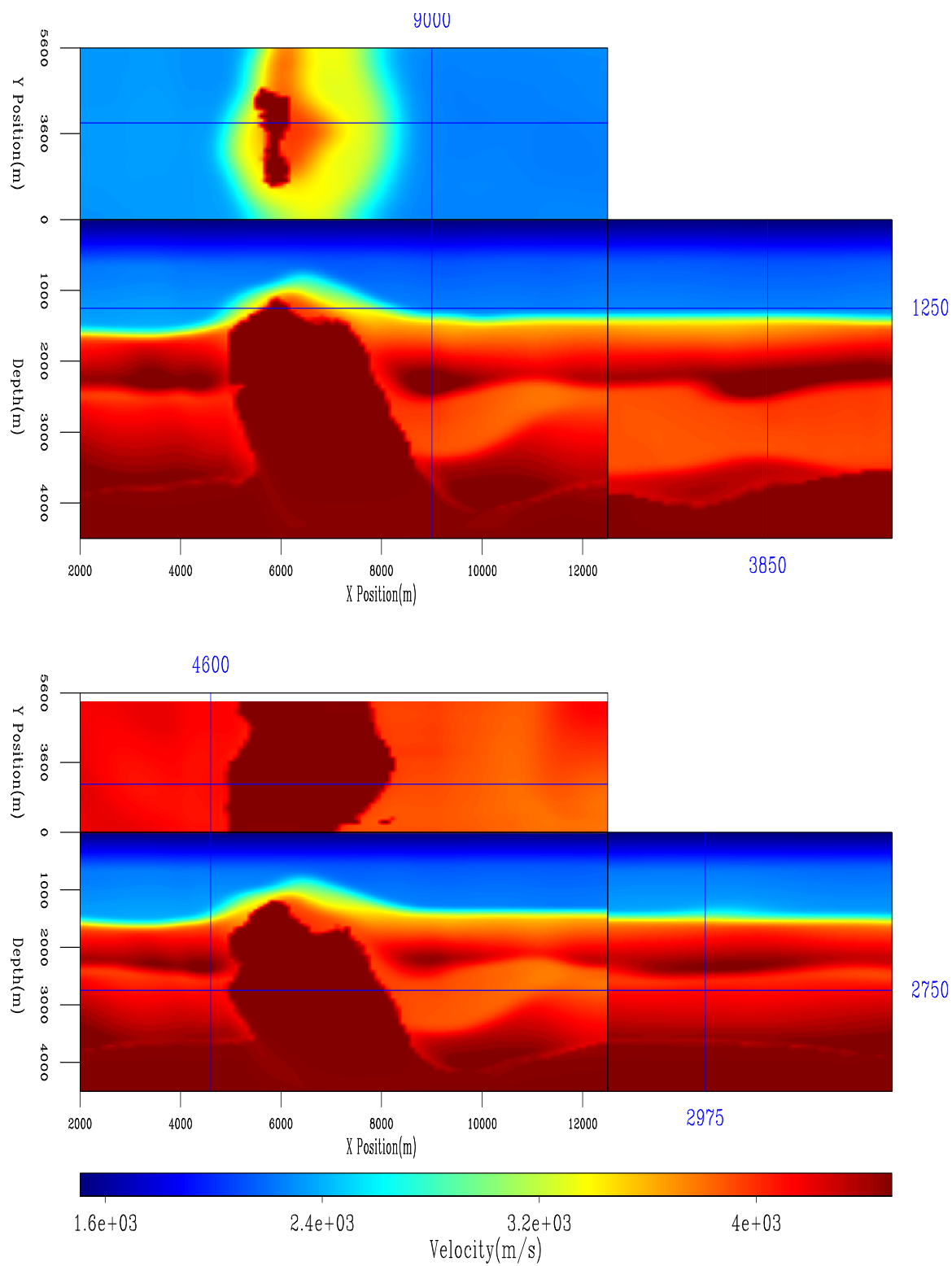


Figure 1.12: Velocity after one iteration of tomography. `3d-elf3d.vel1` [CR]

Migration

I then migrated with the velocity in Figure 1.12. Figures 1.13 and 1.14 show the same two slices through the migration cube as Figures 1.4 and 1.5. Overall image quality is improved. Comparing Figures 1.4 and 1.13 we can see better focusing of the chalk reflector at 'B'. We see more reflectors within the basin structure at 'C'. The fault at 'D' is sharper. In addition, the reflectors under the salt edge are more continuous and extend further.

In the second comparison, Figures 1.5 and 1.14, we see similar improvement. We see better focusing of the chalk reflector at 'B'. The basin reflector ('C') is much better focused. The depth slice shows significantly more structure and better focusing ('E') with the new velocity. The biggest improvement is seen at 'A' and 'D'. At 'A' we again see better continuity and focusing of reflectors under the salt edge. At 'D' little reflector coherence is seen in the initial migration. The migration with the updated velocity shows much more reflector coherence.

Figure 1.15 shows the semblance for the bottom twelve reflectors in the updated image. Generally it was possible to follow the reflectors further than in the initial migration. We also see generally less moveout in the CRP gather than the initial image.

SECOND ITERATION

In an attempt to improve the focusing of the reflectors under the salt edge, I performed another iteration of tomography. This time I concentrated on accurately picking reflectors as close to the salt edge as possible. In addition I relaxed the constraint on model smoothness to allow greater changes. Figure 1.16 shows the updated velocity model. The changes introduced to the velocity model are significantly greater than in the first iteration of tomography (Figures 1.11 and 1.12).

If we look at the same two cube views (as Figures 1.3, 1.4, 1.5, 1.16, 1.13, 1.14, and 1.16), we see improved focusing of the reflectors, especially as we approach the salt edge. In Figure 1.17 note the improvement over Figures 1.4 and 1.13 at 'A', 'C' and 'D'. In Figure 1.18 we see improvements over Figures 1.5 and 1.14 at the same general locations ('A', 'C' and D).

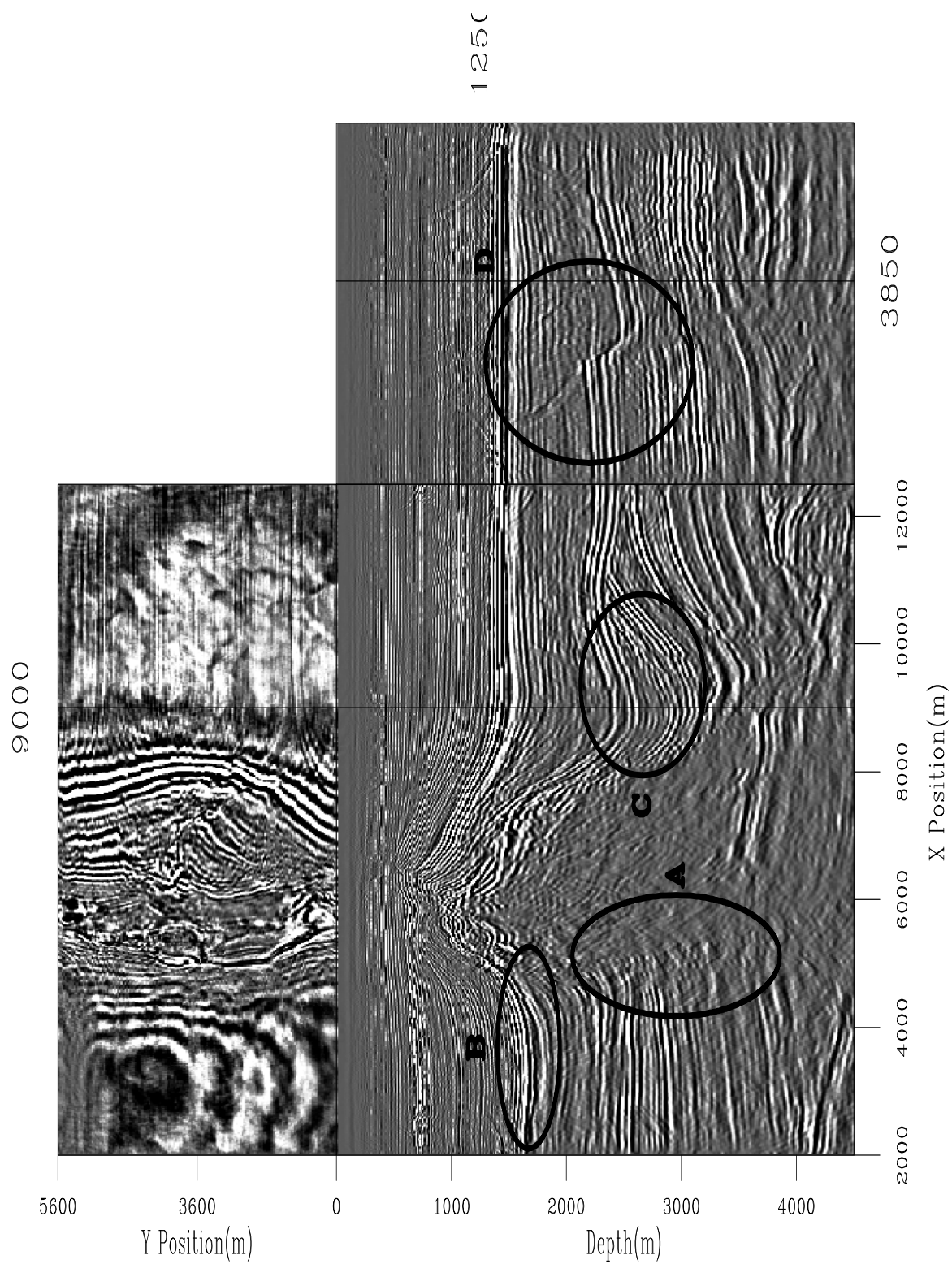


Figure 1.13: Slice through the migrated cube using the velocity of Figure 1.12.
 3d-cube.mig1.1 [CR,M]

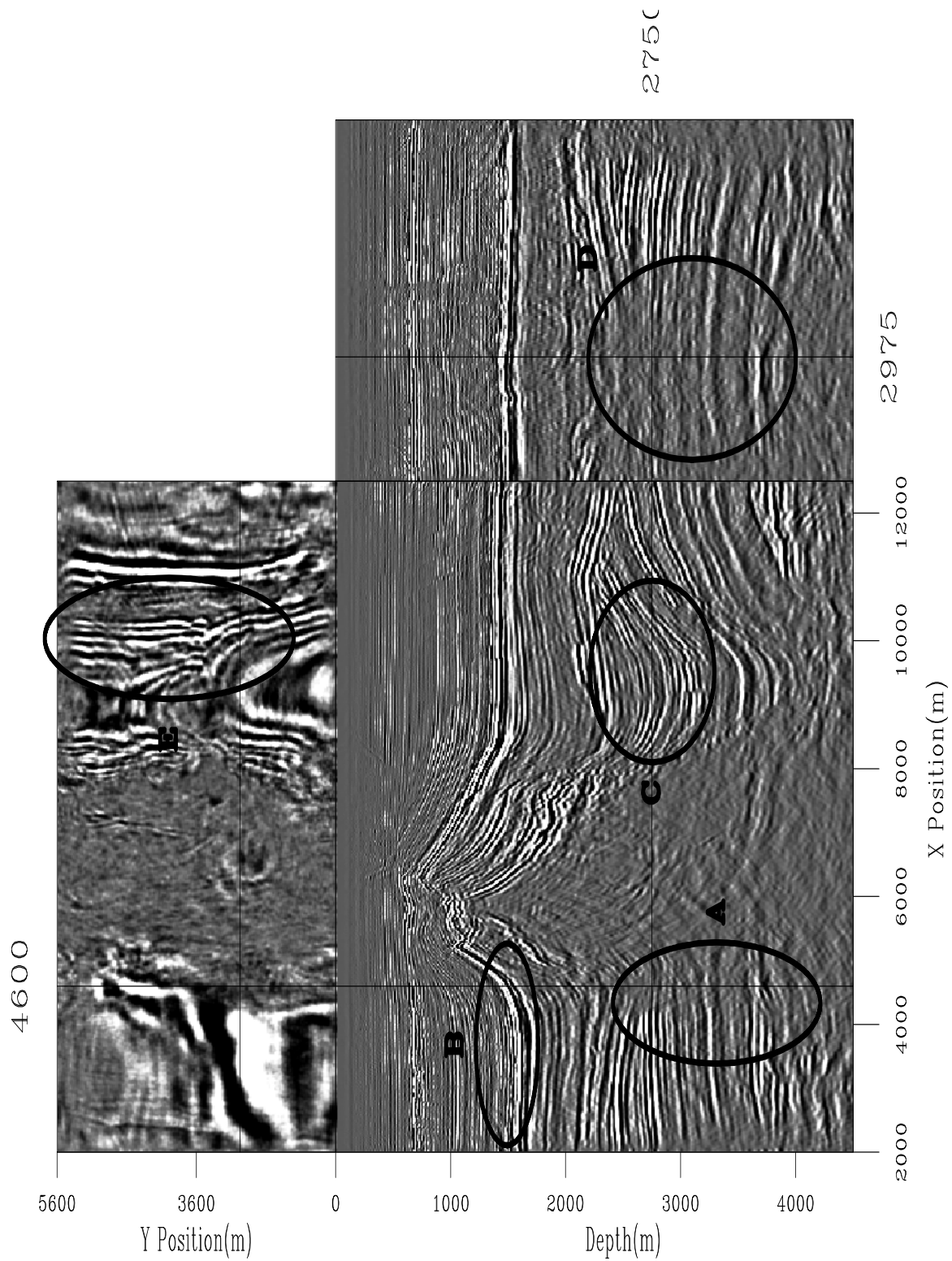


Figure 1.14: A second slice through the migrated cube using the velocity of Figure 1.12.
 3d-cube.mig1.2 [CR,M]

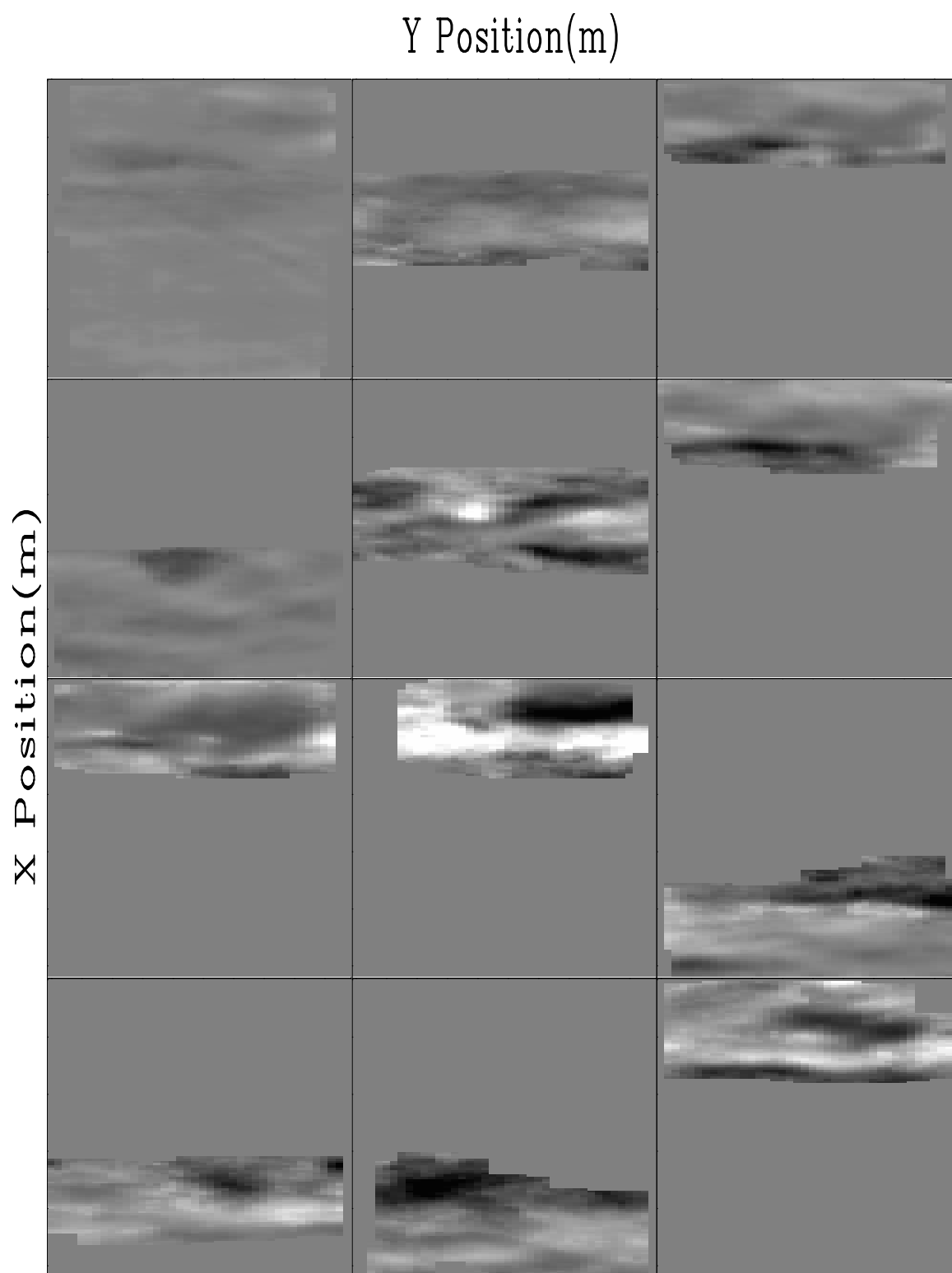


Figure 1.15: Picked semblance along the bottom 12 reflectors used in tomography.
`3d-smooth.3d.vell` [CR,M]

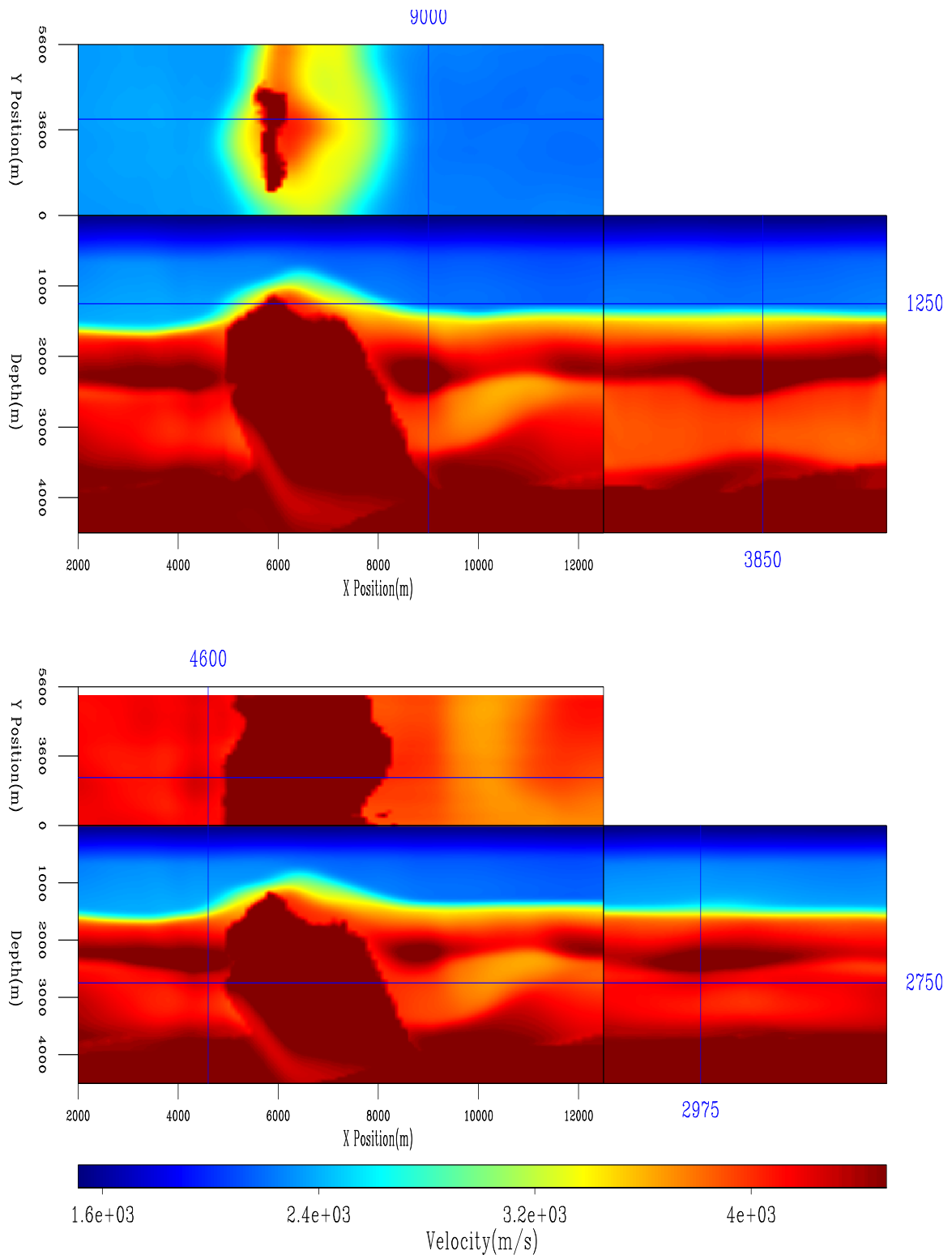


Figure 1.16: Velocity after two iterations of tomography. `3d-elf3d.vel2` [CR]

If we look at the gathers from the same crossline as Figure 1.6 (Figure 1.19) we see that they considerably flatter and more coherent than in the initial migration.

If we take a close up view of the area to the left of the salt, Figure 1.20, the improvement in image quality is very apparent. The salt bottom reflector ('A') is more continuous. The reflectors along the edge of the salt ('B') extend almost to the edge of the salt and are much more consistent in amplitude. In the crossline view we see reflector continuity ('C') that was not apparent in the initial image.

A close up view of the right portion of the image Figure 1.21 also shows improvement. The strong reflector above the salt ('A') is discontinuous with the initial velocity model, with the improved velocity model it is much more believable. The reflectors in the basin to the right of the salt 'D' are more consistent in amplitude. The fault in the crossline 'C' is better focused and we have generally more energy in the crossline reflectors below the fault. Finally, the depth section 'B' is higher frequency and shows more continuous reflectors.

2-D vs. 3-D

As a final comparison I extracted the crossline corresponding to the 2-D tomography/migration of Chapter ???. Figure 1.22 shows a blowup of the lower portion of both images. Note how the 3-D result is almost universally better. The lower salt edge reflectors continue further in the 2-D case, but are not as consistent in amplitude or as well focused. The upper salt edge reflectors are better focused in 3-D case. The salt bottom in the 3-D case is of higher amplitude, and more consistent than its 2-D counterpart. To the right of the salt the improvements are even more dramatic. The chalk reflectors are much better imaged in 3-D case. The basin structure is better focused in 3-D case, and below the basin we see many more coherent events than in the 2-D migration.

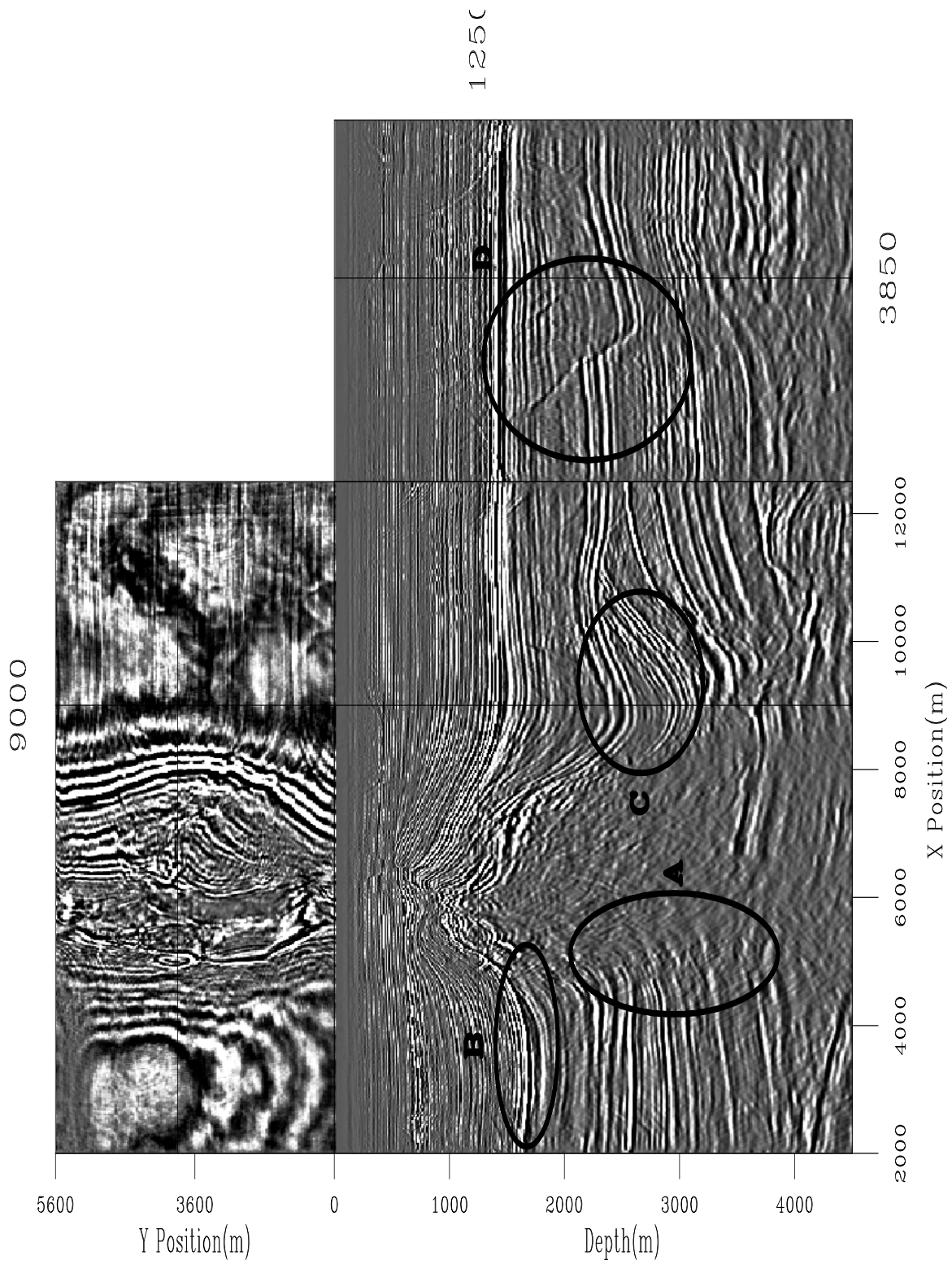


Figure 1.17: Slices from the 3-D cube using the velocity of Figure 1.16 3d-cube.mig2.1 [CR,M]

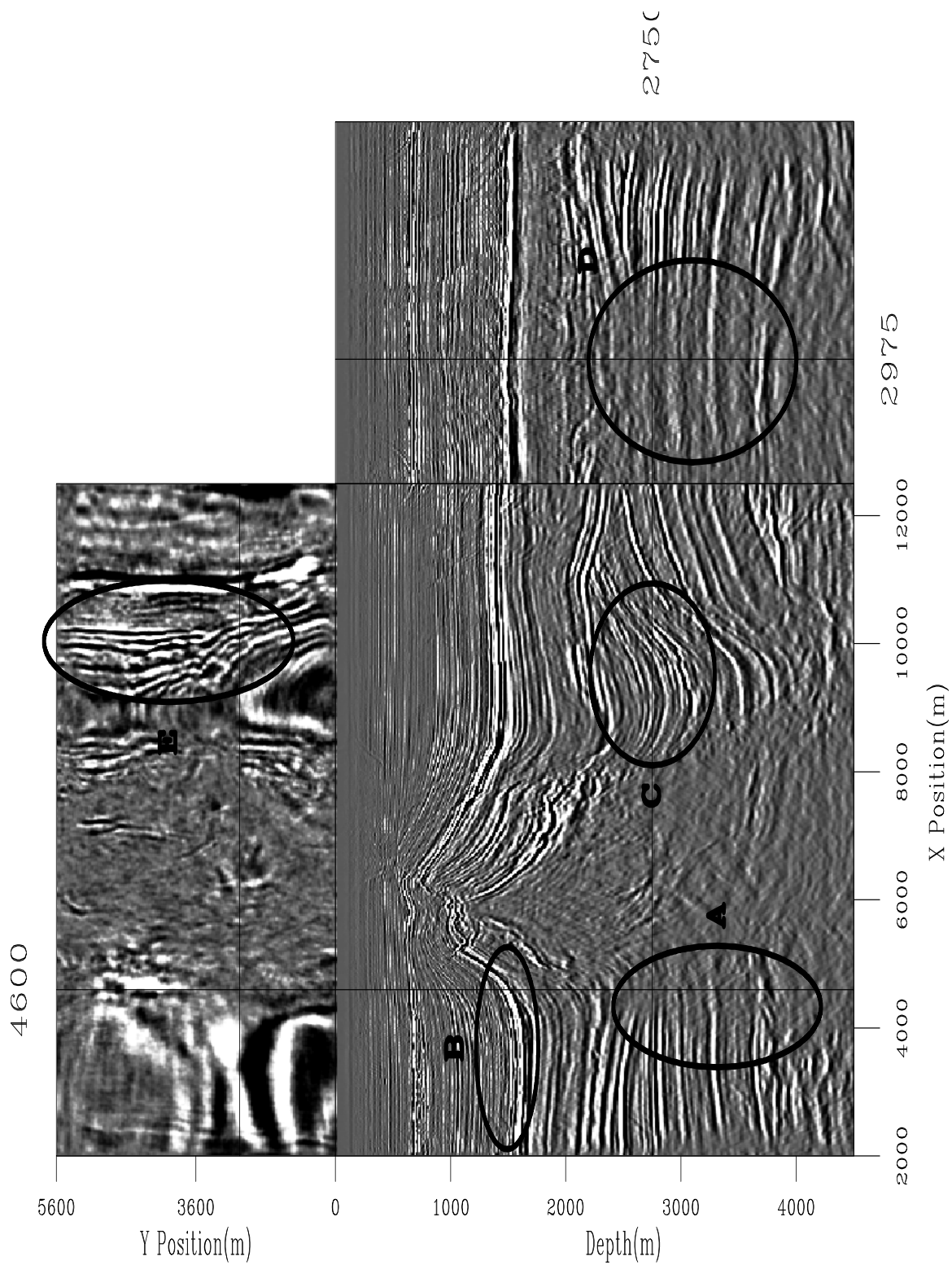


Figure 1.18: Slices from the 3-D cube using the velocity of Figure 1.16 3d-cube.mig2.2 [CR,M]

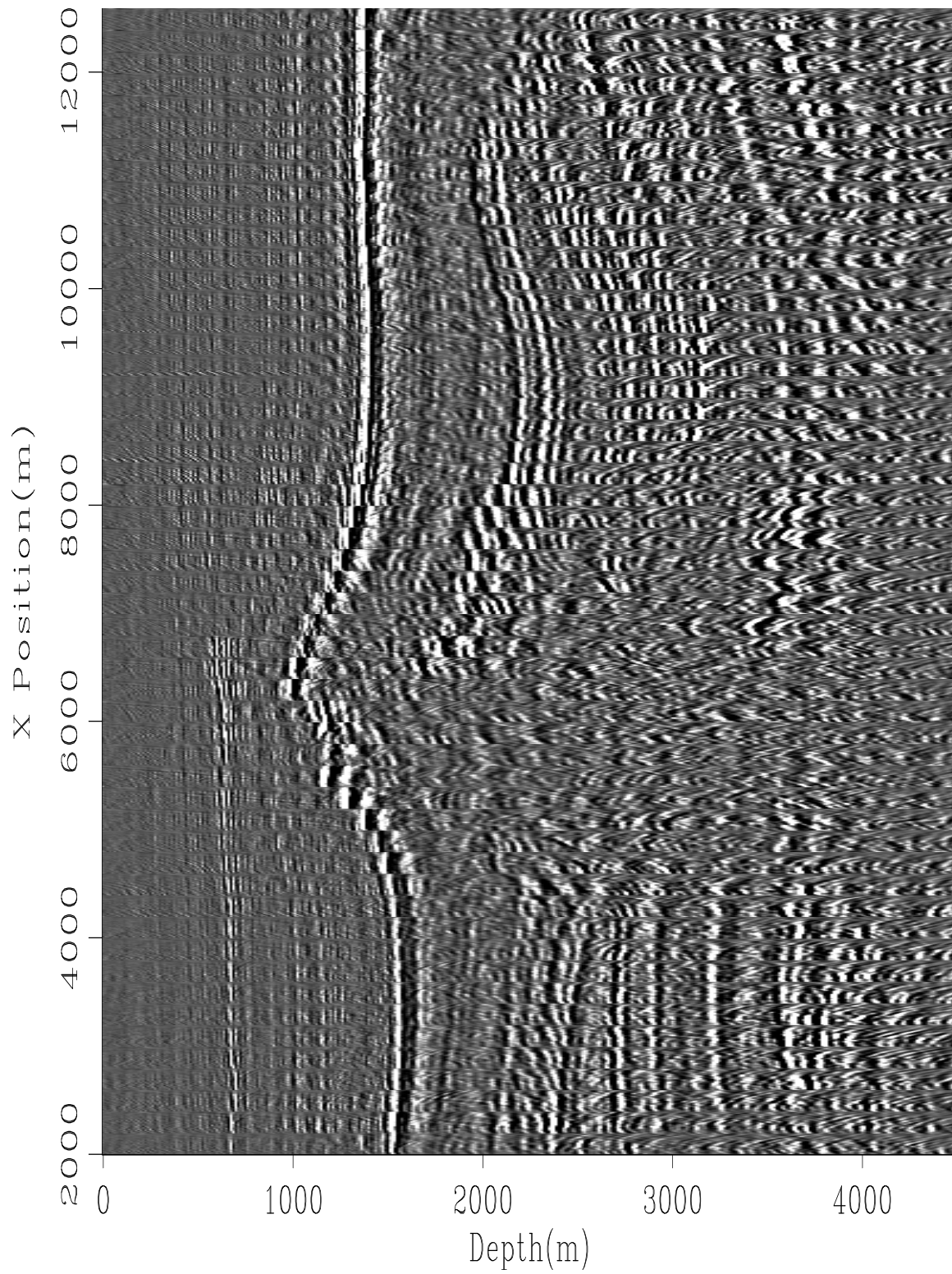


Figure 1.19: Gathers from the same crossline as Figure 1.6. `3d-gathers.3d.vel2` [CR,M]

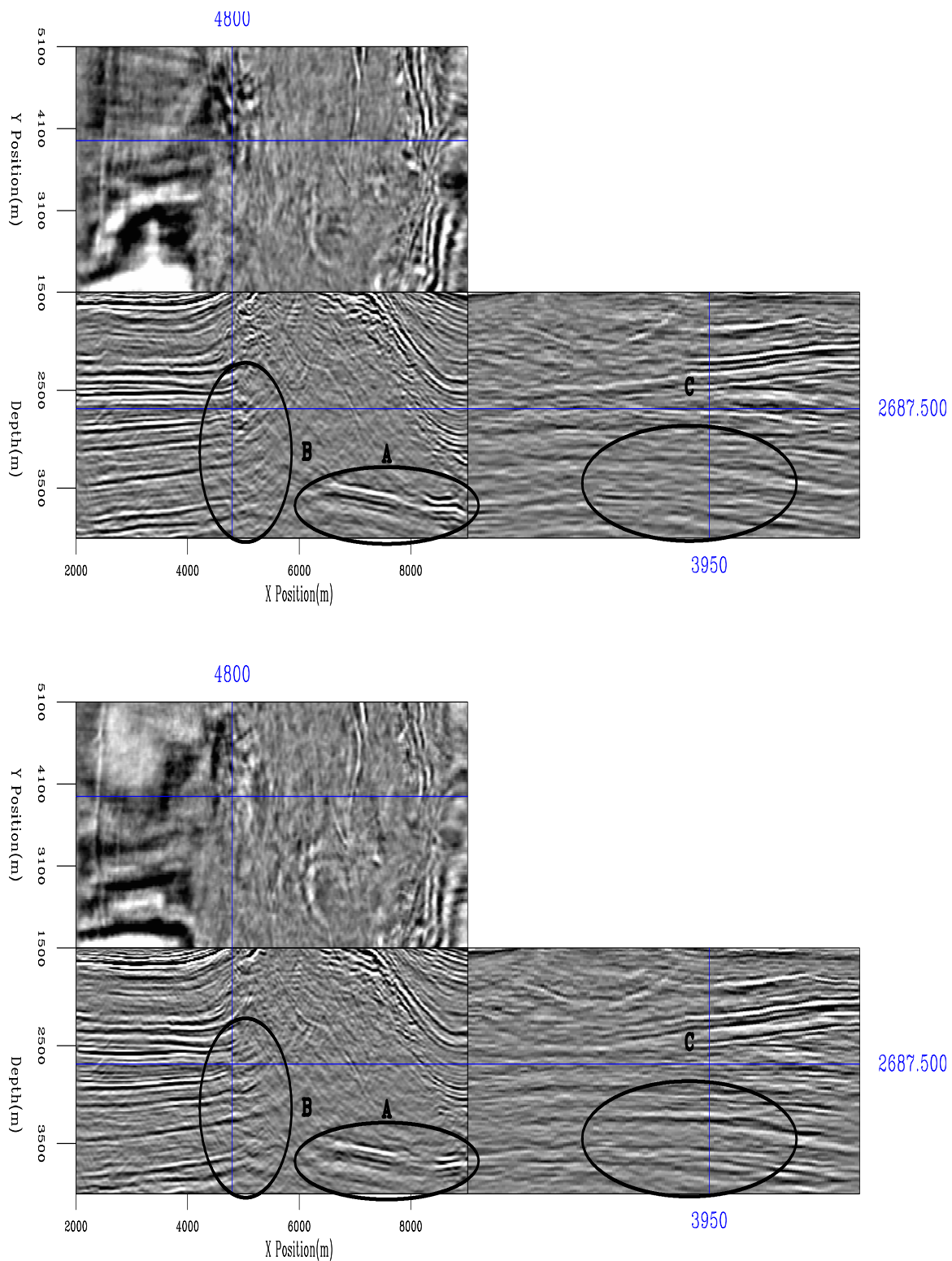


Figure 1.20: A comparison along the left edge of the salt dome. The top image is using the starting velocity, Figure 1.3, the bottom using the velocity after two iterations (Figure 1.16).

3d-compare1 [CR,M]

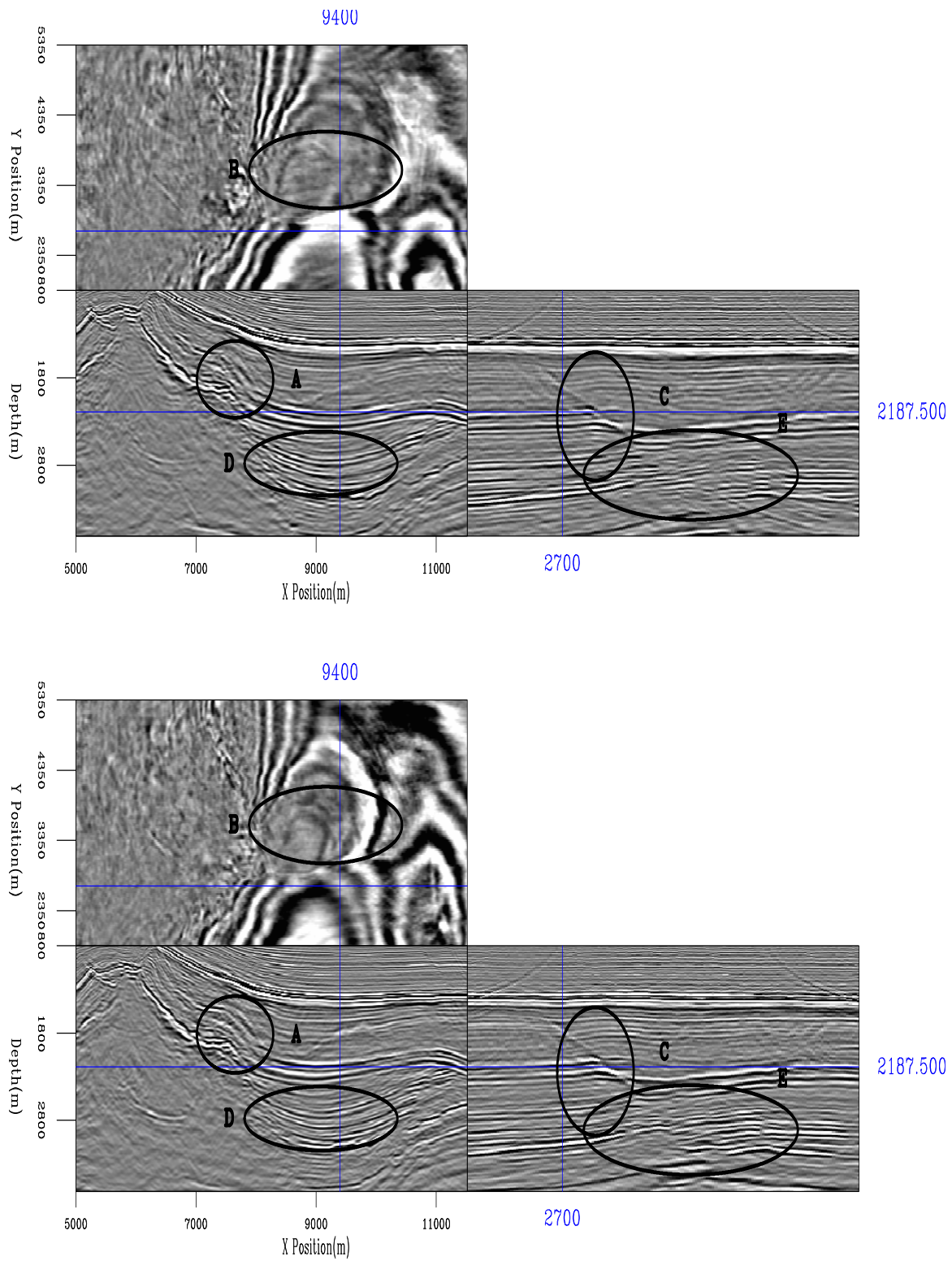


Figure 1.21: A comparison along the right edge of the salt dome. The top image is using the starting velocity, Figure 1.3, the bottom using the velocity after two iterations (Figure 1.16).

3d-compare2 [CR,M]

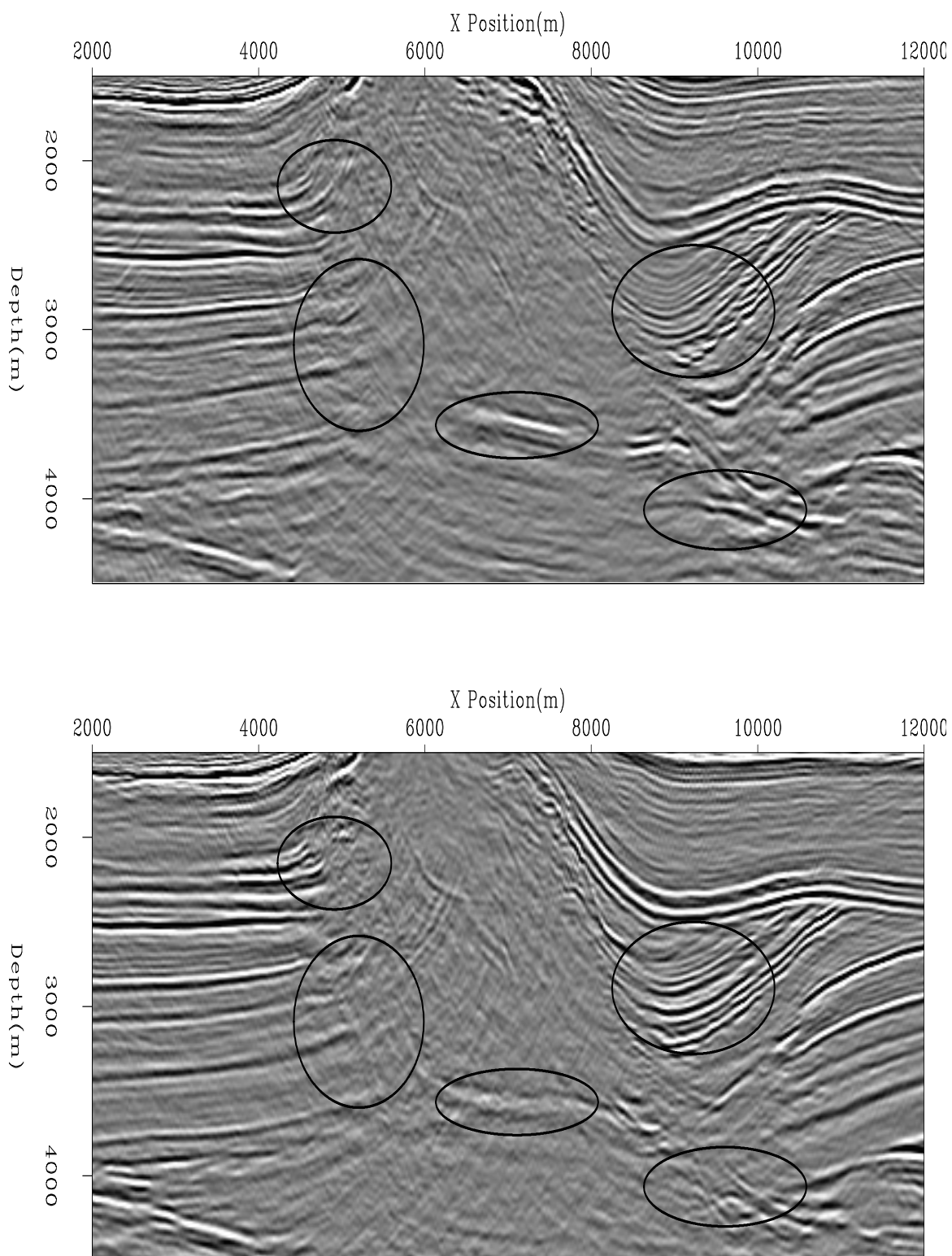


Figure 1.22: A comparison of the 2 and 3-D tomography/migration result. The bottom image is the best migration result from Chapter ???. The top figure is the same crossline, taken from 3-D migration/tomography result. [3d-3d-vs-2d](#) [CR,M]

Bibliography

- Biondi, B., and Palacharla, G., 1996, 3-D prestack migration of common-azimuth data: *Geophysics*, **61**, no. 6, 1822–1832.
- Biondi, B., Fomel, S., and Chemingui, N., 1998, Azimuth moveout for 3-D prestack imaging: *Geophysics*, **63**, no. 2, 574–588.
- Biondi, B., Clapp, R. G., and Rickett, J., 1999, Testing linux multiprocessors for seismic imaging: *SEP*–**102**, 235–248.
- Biondi, B. L., 1999, 3-D Seismic Imaging: Stanford Exploration Project.
- Ehinger, A., and Lailly, P., 1995, Velocity model determination by the SMART method, part 1: Theory: 65th Annual Internat. Mtg., Soc. Expl. Geophys., Expanded Abstracts, 739–742.
- Hale, I. D., 1983, Dip moveout by Fourier transform: Ph.D. thesis, Stanford University.
- Hanson, D. W., and Witney, S. A., 1995, 3-D prestack depth migration – velocity model building and case history: 1995 Spring Symposium of the Geophys. Soc. of Tulsa, Soc. Expl. Geophys., Seismic Depth Estimation, 27–52.
- Jacobs, J. A. C., Delprat-Jannaud, F., Ehinger, A., and Lailly, P., 1992, Sequential migration-aided reflection tomography: A tool for imaging complex structures: 62nd Annual Internat. Mtg., Soc. Expl. Geophys., Expanded Abstracts, 1054–1057.
- Mosher, C. C., Foster, D. J., and Hassanzadeh, S., 1997, Common angle imaging with offset plane waves: 67th Annual Internat. Mtg., Soc. Expl. Geophys., Expanded Abstracts, 1379–1382.

- Ottolini, R., and Claerbout, J. F., 1984, The migration of common-midpoint slant stacks: *Geophysics*, **49**, no. 3, 237–249.
- Ronen, J., 1985, Multichannel inversion in reflection seismology: *SEP*–**46**.
- Vaillant, L., and Biondi, B., 2000, Accuracy of common-azimuth migration approximations: *SEP*–**103**, 157–168.
- Vaillant, L., and Calandra, H., 2000, Common-azimuth migration and Kirchhoff migration for 3-D prestack imaging: A comparison on North Sea data: *SEP*–**103**, 139–147.
- Vaillant, L., and Sava, P., 1999, Common-azimuth migration of a North Sea dataset: *SEP*–**102**, 1–14.